UC Davis
UC Davis Previously Published Works

Title

Oxygen trapped by rare earth tetrahedral clusters in Nd4FeOS6: Crystal structure, electronic structure, and magnetic properties

Permalink

https://escholarship.org/uc/item/7z96830z

Authors

Lin, Qisheng
Taufour, Valentin
Zhang, Yuemei
et al.

Publication Date

2015-09-01

DOI

10.1016/j.jssc.2015.05.020

Peer reviewed

Oxygen trapped by rare earth tetrahedral clusters in Nd_4FeOS_6: Crystal structure, electronic structure, and magnetic properties

Qisheng Lin [a,*], Valentin Taufour [a,b], Yuemei Zhang [c], Max Wood [a,b], Thomas Drtina [a,b], Sergey L. Bud'ko [a,b], Paul C. Canfield [a,b], Gordon J. Miller [a,c]

[a] Division of Materials Sciences and Engineering, Ames Laboratory, US-DOE, Ames, IA 50011, USA
[b] Department of Physics and Astronomy, Iowa State University, Ames, IA 50011, USA
[c] Department of Chemistry, Iowa State University, Ames, IA 50011, USA

ABSTRACT

Single crystals of Nd_4FeOS_6 were grown from an Fe–S eutectic solution. Single crystal X-ray diffraction analysis revealed a Nd_4MnOSe_6-type structure ($P6_3mc$, $a=9.2693(1)$ Å, $c=6.6650(1)$Å, $V=495.94(1)$ Å^3, $Z=2$), featuring parallel chains of face-sharing $[FeS_{6\times1/2}]^{4-}$ trigonal antiprisms and interlinked $[Nd_4OS_3]^{4+}$ cubane-like clusters. Oxygen atoms were found to be trapped by Nd_4 clusters in the $[Nd_4OS_3]^{4+}$ chains. Structural differences among Nd_4MnOSe_6-type Nd_4FeOS_6 and the related La_3CuSiS_7- and Pr_8CoGa_3-type structures have been described. Magnetic susceptibility measurements on Nd_4FeOS_6 suggested the dominance of antiferromagnetic interactions at low temperature, but no magnetic ordering down to 2 K was observed. Spin-polarized electronic structure calculations revealed magnetic frustration with dominant antiferromagnetic interactions.

© 2015 Elsevier Inc. All rights reserved.

1. Introduction

The study of $3d/4f$ systems has long been a focus of research in crystallography, materials chemistry, physical metallurgy, and condensed matter physics because of their structural richness and physical diversity[1–9]. Metal-rich compounds containing both itinerant d electrons of transition metals and more localized f electrons of rare earth metals may yield large $3d$–$4f$ exchange interactions that offer potential for many applications such as permanent magnets [7, 8, 10]. With the goal of discovering new ferromagnetic materials, we are focusing on the Fe-rich part of the ternary RE–Fe–X (RE=Nd, Dy and X=S, Sb, Ge) phase spaces [11]. If any new Fe-rich compounds exist and decompose peritectically at a rather low temperature compared with the melting point of Fe, it can be difficult to obtain from directly arc-melting mixtures of elements or by using traditional heating procedures. In addition, the high vapor pressures of sulfur and antimony, in particular, make arc-melting even less practical.

Therefore, we turned to a solution growth technique, which has proved to be quite practical for growing high quality single crystals at relatively low temperatures [12–14]. During exploration of the Nd–Fe–S system, we found that the Fe-rich eutectic liquid of the Fe–S binary system, that is, $Fe_{55\pm2}S_{45\mp2}$ could be safely heated up to

1150 °C without any detectable sulfur outside the crucible as long as Fe powder (as opposed to large Fe pieces) was used as a reactant. Herein, we report the synthesis, structure, and magnetic susceptibility of an unexpected quaternary product, Nd_4FeOS_6 (space group $P6_3mc$), which is structurally similar to Nd_4FeS_7 ($P6_3$) [15]. However, the structural variations arising from the incorporation of oxygen atoms are distinct, and include large differences in lattice parameters and bonding patterns.

2. Experimental

2.1. Synthesis

Reactants used for crystal growth include elemental Nd lumps (99.999%, Ames Laboratory), Fe powder (< 10 µm, 99.9%, Alfa Aesar), and S powder (99.999%, Alfa Aesar). A mixture with initial stoichiometry "$Nd_4Fe_{55}S_{41}$" was introduced into a 2 ml alumina crucible, sealed in a fused silica ampoule, and heated at 300 °C for 3 h, followed by a slow heating over 12 h to 1150 °C to ensure that Fe and S form a near eutectic melt. The melt was then slowly cooled to 1000 °C at a rate of 1 °C/h. The ampoule was then taken out of the furnace at 1000 °C, inverted in the cup of a centrifuge and quickly spun to separate crystals from the remaining liquid [13].

Single crystals of several phases grew. In addition to

compounds bearing Nd, Fe, and S, we found two oxygen-bearing compounds: the known $Nd_{10}S_{14}O$ [16] in cuboid shape and the new title phase Nd_4FeOS_6 in rod shape. The oxygen necessary to form these phases most likely originated as mild surface oxidation of the elemental Nd and Fe. Although such an oxide contamination often forms an insoluble slag layer on the surface of many inter-metallic melts, in the case of this Fe–S based melt, oxygen is clearly soluble to some degree. However, it was not our attempt to target the title new material through conventional solid-state synthesis, which was successfully applied for isostructural phases such as RE_4MnOSe_6 (RE=La, Ce, Nd), RE_4FeOSe_6 (RE=La, Ce, Sm), and La_4MnOS_6 [17].

2.2. Single crystal X-ray diffraction

Single crystal diffraction data for both $Nd_{10}S_{14}O$ and Nd_4FeOS_6 crystals were collected at room temperature using a Bruker SMART APEX II diffractometer equipped with Mo K_α radiation ($\lambda=0.71073$ Å) over a 2θ range of ~3° to ~60° in mixed ω and φ scan modes and exposure times of 10 s per frame. Intensity data were integrated with the SAINT program [18]. Empirical absorption corrections were made with the aid of SADABS [19]. Structure determination and least-squares refinements were carried out using SHELXTL 6.1 [20]. According to our analyses, the crystallographic data of $Nd_{10}S_{14}$ ($I4_1/acd$, $a=15.0003$ (1) Å, $c=19.9040$ (2) Å, $Z=8$) are close to the ones reported in the literature ($a=15.0380$ (4) Å, $c=19.9646$ (8) Å) [16]. The rod-shaped crystals, which turned out to be a new phase, were refined as Nd_4FeOS_6, space group $P6_3mc$, and lattice parameters $a=9.2693(1)$ Å, $c=6.6650(1)$ Å, $V=495.94(1)$ Å^3, $Z=2$.

The structural solution of Nd_4FeOS_6 in the space group $P6_3mc$ was quite straightforward except that the assignment of oxygen atoms needs special attention. At first, direct methods yielded four sites showing reasonable interatomic distances; they were assigned as Nd1, Nd2, Fe, and S1 based on respective bond distances and peak intensities. After a few cycles of least-squares refinements, two additional sites were suggested by the difference Fourier map, so they were assigned as S2 and S3. Subsequent refinement converged smoothly to R1=0.044. However, the U_{eq} value (0.078 Å^2) for S3 at the Wyckoff 2b site was ~9 times larger than the average value (0.009 Å^2) of the S1 and S2 atoms, suggesting a partial occupancy of S at the S3 site. So the occupancy of S3 was refined in subsequent least-squares refinements, which yielded R1=0.042, together with an occupancy of 57(8) % and U_{eq} of 0.038 Å^2 for S3. The refinements with anisotropic displacement parameters converged at R1=0.0147, wR2=0.0319, GOF=1.043, max./min. residual peaks of 1.10/−0.79 e/Å^3, and a composition of $Nd_4FeS_{6.55(2)}$. But still, S3 at the 2b site had a considerably large U_{eq} value of (0.030 Å^2) and a noticeably short distance to neighboring Nd1 atoms (2.333 Å).

At this stage, we realized that the foregoing structure and composition were close to that of Nd_4FeS_7, [15] which has a lower symmetry $P6_3$, larger lattice constant a (10.098 versus 9.269 Å), smaller c (5.524 versus 6.665 Å), and smaller unit cell volume (487.82 versus 495.94 Å^3). These values apparently contradict a general rule that the lattice constants and volume of a crystal with refined vacancies should be smaller than the same crystal without vacancies, suggesting that the assignment of S to the Wyckoff 2b site could be incorrect. Since oxygen had been shown to be present in $Nd_{10}S_{14}O$ obtained from the same reaction, we speculated that the Wyckoff 2b site could be occupied by oxygen, which is reasonable in terms of both peak intensity and bond distance to neighboring Nd atoms. Therefore, the ensuing least-squares refinements assigning O to the 2b site yielded slightly smaller R values (R1=0.0145, wR2=0.0302), a reasonable U_{eq} value for the O atom (0.008 Å^2), and a composition of Nd_4FeOS_6. In the Results

and discussion section, we will provide additional evidence to support the assignment of oxygen rather than sulfur at the 2b site, including bond valences and a comparison of c/a ratios among related phases.

Because Nd_4FeOS_6 adopts an acentric space group, Platon [21] was used to check possible missing symmetry elements after final least-squares refinements, but no higher symmetry space groups were suggested. One possible concern is that the U_{eq} value of Nd2 atom is about 2.5 times larger than that of Nd1 [0.023(1) Å^2 versus 0.009(1) Å^2] and its U_{11} and U_{22} tensor values are ~5 times that of U_{33}; however, independent refinements to check its occupancy reveal fully occupancy. Therefore, the large displacement parameter for Nd2 could originate from its environment. In fact, Nd2 is located in a tricapped-tetrahedron with long interatomic separations (3.404 Å) to the three S capping atoms (see below). Details of the data collection and structural refinements for Nd_4FeOS_6 are summarized in Table 1. Atomic positions standardized by STRUC-TURE TIDY [22] and equivalent isotropic displacement parameters are given in Table 2. Selected interatomic distances are listed in Table 3. Other detailed crystallographic data are provided in the CIF file in the Supporting information.

2.3. Physical properties measurements

Magnetization measurements from 2 K to 300 K were performed using a Quantum Design, Magnetic Property Measurement System (MPMS) superconducting quantum interference device magnetometer at different magnetic fields (20 Oe, 2 T and 4 T). Attempts to measure the electrical resistivity of samples using the four-probe method were also made, but the results indicated insulating behavior for Nd_4FeOS_6.

2.4. Electronic structure calculations

The electronic structure and total energies of various

Table 1
Crystal data and structure refinement for Nd_4FeOS_6.

Empirical formula	Nd_4FeOS_6
Formula weight	841.17
Space group	$P6_3mc$
Unit cell dimensions	$a=9.2693$ (1) Å
	$c=6.6650$ (1) Å
Volume	495.94(1) Å^3
Z	2
Density (calculated)	5.633 Mg/m^3
Absorption coefficient	23.194 mm^{-1}
Reflections collected/R_{int}	7208/0.0486
Data / restraints/parameters	567/0/29
Goodness-of-fit on F^2	1.069
Final R indices [I > 2sigma(I)]	R1=0.0145, wR2=0.0302
R indices (all data)	R1=0.0149, wR2=0.0303
Absolute structure parameter	−0.01(3)
Extinction coefficient	0.0221(7)
Largest diff. peak and hole	1.145 and −0.835 e.Å^{-3}

Table 2
Atomic coordinates and equivalent isotropic displacement parameters for Nd_4FeOS_6. U(eq) is defined as one third of the trace of the orthogonalized U^{ij} tensor.

Atom	Wyckoff.	Site symm.	x	y	z	Ueq (Å^2)
Nd1	6 c	.m.	0.8024(1)	−x	0.1700(3)	0.009(1)
Nd2	2 b	3 m.	1/3	2/3	0.2021(3)	0.023(1)
Fe	2 a	3 m.	0	0	0	0.013(1)
S1	6 c	.m.	0.1231(1)	−x	0.2686(5)	0.010(1)
S2	6 c	.m.	0.5303(1)	−x	0.4480(5)	0.013(1)
O	2 b	3 m.	1/3	2/3	0.545(2)	0.007(2)

Table 3
Selected interatomic distances in the structure of Nd_4FeOS_6.

Atom pair	Distances (Å)	Atom pair	Distances (Å)
Nd1–O	2.333(4)	Fe–S1	2.507(2)
Nd2–O	2.29(1)	Fe–S1	2.667(3)
Nd1–S1	2.8516(6)	Nd1–Fe	3.3685(7)
Nd1–S1	2.930(2)	Nd1–Nd1	3.7747(5)
Nd1–S2	2.864(2)	Nd1–Nd2	3.8042(8)
Nd1–S2	3.170(2)	Nd2–S2	2.768(2)

magnetically ordered models of Nd_4FeOS_6 were calculated using the projector augmented wave method (PAW) of Blöchl [23, 24] coded in the Vienna *ab initio* simulation package (VASP) [25, 26]. All VASP calculations employed the generalized gradient approximation (GGA) with exchange and correlation treated by Perdew–Burke–Enzerhoff (PBE)[27]. The linear spin density approximation (LSDA) including on-site Hubbard repulsion U parameters (LSDA+U) [28] were adopted to describe electron correlations associated with Nd 4f states and Fe 3d states. As before, [29, 30] $U_{\mathrm{eff}}=6.0$ eV for Nd 4f states was adopted in this case, together with $U_{\mathrm{eff}}=3.0$ eV for Fe 3d states that properly opens a gap in the electronic density of states (DOS) at the Fermi level. Nevertheless, calculations with $U_{\mathrm{eff}}=4.0$ eV for Fe 3d states were also tried, and similar outcomes among the differences of total energies for various magnetic models were observed as that for $U_{\mathrm{eff}}=3.0$ eV. The cutoff energy for the plane wave calculations was set to 500 eV and the Brillouin zone integration was carried out using $6\times6\times9$ Γ-centered $\boldsymbol{k}$-point meshes.

3. Results and discussion

3.1. Structure

Nd_4FeOS_6, with space group $P6_3mc$, Pearson symbol $hP24$, and Wyckoff sequence c^3b^2a, belongs to the recently found family of Nd_4MnOSe_6-type structures, which include only seven oxychalcogenides, viz., RE_4MnOSe_6 (RE=La, Ce, Nd), RE_4FeOSe_6 (RE=La, Ce, Sm) and La_4MnOS_6 [17]. This structure type is the anti-type of $K_5InTe_4 \cdot KCl$ [31], which may be reformulated as Te_4ClInK_6 to emphasize this type/anti-type relationship. The title phase also resembles Nd_4FeS_7,[6] which crystallizes in the space group $P6_3$ and has lattice parameters $a=10.098$ Å and $c=5.524$ Å.

Fig. 1 shows the coordination environments of the two independent Nd atoms in Nd_4FeOS_6. Each Nd1 atom is six-coordinated by one O with $d_{\mathrm{Nd1-O}}=2.333(4)$ Å, three S1 with $d_{\mathrm{Nd1-S1}}=2.8518(6)–2.930(2)$ Å, and two S2 atoms with $d_{\mathrm{Nd1-S2}}=2.864(2)$ Å. These six atoms form a trigonal prism, of which the two S1–S1–S2–O faces are capped by additional S2 atoms at a distance of $d_{\mathrm{Nd1-S2}}=3.170(2)$ Å. In comparison, Nd2 is surrounded by a tetrahedron consisting of one oxygen ($d_{\mathrm{Nd2-O}}=2.28(1)$ Å) and three S2 ($d_{\mathrm{Nd2-S2}}=2.768(2)$ Å) atoms. All three O–S2–S2 triangular faces are further capped by S1 atoms with $d_{\mathrm{Nd2-S1}}=3.404(4)$ Å. The orientation of this particular coordinating environment allows larger U_{ij} tensor values in the ab-plane for the central Nd2 atoms, resulting in a reasonably large U_{eq} value as listed in Table 2. The packing of $Nd1S_7O$ and $Nd2S_6O$ polyhedra generate a three-dimensional framework with hexagonal tunnels located at (0 0 z), Fig. 2. These tunnels are filled by Fe atoms, which form one-dimensional $_\infty[1]$ $[FeS_{6\times1/2}]^{4-}$ chains.

As shown in Fig. 3, the structure of Nd_4FeOS_6 can also be described as a packing of two types of chains running along the c-axis: $_\infty[1]$ $[FeS_{6\times1/2}]^{4-}$ chains at (0 0 z) and equivalent sites and $_\infty[1]$ $[Nd_4OS_3]^{4+}$ chains at (1/3 2/3 z) and equivalent sites. The
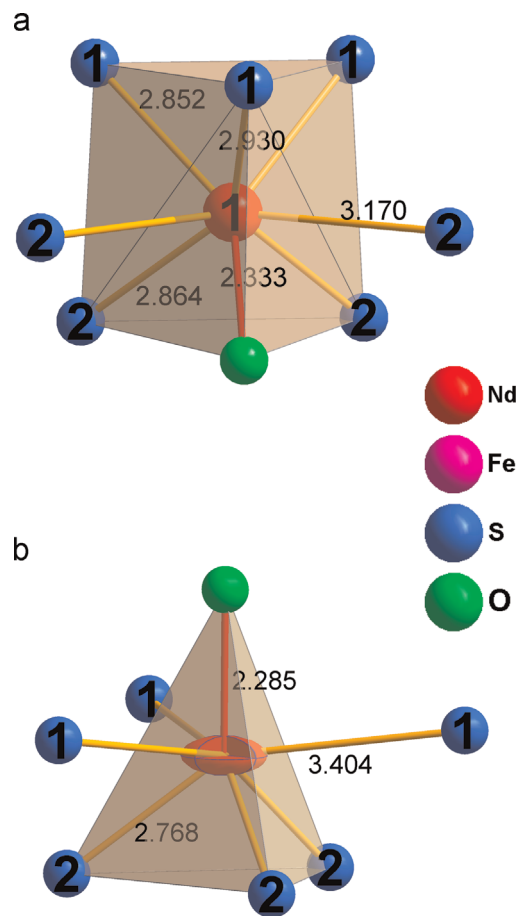
Fig. 1. Environments of (a) Nd1 and (b) Nd2 in the structure of Nd_4FeOS_6. Numbers in spheres denote independent atoms as listed in Table 2.

former chains consist of face-sharing $[FeS_6]^{4-}$ trigonal antiprisms, each having two sets of Fe–S1 distances, 2.507(2) Å and 2.667(3) Å. The Fe–Fe distance along the chain is 3.333(1) Å, one-half of the lattice constant c, and a distance probably too long to be considered as Fe–Fe bonding. In comparison, the Fe–Fe distance (2.762 Å=½c) in Nd_4FeS_7 is about 0.6 Å shorter, indicating a possible through-space Fe–Fe bonding interaction. Such differences could result in different Fe–Fe exchange interactions and subsequent magnetic properties between these two phases.

The $_\infty[1]$ $[Nd_4OS_3]^{4+}$ chain can be viewed as a packing of $[Nd_4OS_3]^{4+}$ cubane-like clusters that are interlinked by Nd2–O bonds. The $[Nd_4OS_3]^{4+}$ cluster resembles the geometry of well-known $[Fe_4S_4]$ clusters, [32, 33] which are important metal clusters in metallo-biomolecules. The $_\infty[1]$ $[Nd_4OS_3]^{4+}$ chain may also be described as a chain of Nd_4O tetrahedra bridged by S1 atoms. The center-to-vertex distances in $[Nd_4O]$ tetrahedra are 2.29(1) Å for O–Nd2 and 2.334(4) Å for O–Nd1, comparable to that in Nd_2O_3 (2.303 Å), [34] $Nd_{10}S_{14}O$ (2.408 Å), [16] and Nd_4MnOSe_6 (2.33–2.36 Å) [35]. If the oxygen site (2b) is assigned to a sulfur atom, unreasonably short bond distances to Nd1 and Nd2 will result. According to the bond valence method, [36] the calculated bond valence sum (BVS) for three O–Nd1 and one O–Nd2 bonds in Nd_4FeOS_6 is 2.09, whereas that for three S–Nd1 and one S–Nd2 in $Nd_4Fe("S")S_6$ is unreasonably high (8.29). This result further supports that it is oxygen and not sulfur located at the center of Nd_4 tetrahedra. The Nd1–Nd1 and Nd1–Nd2 distances within each $[Nd_4O]$ tetrahedron are, respectively, 3.7748(6) Å and 3.8043(8) Å, close to those in Nd_4MnOSe_6 [3.8061 (9) Å and 3.835(1) Å] [35].

The various interatomic distances and structural configurations involving the magnetically active Nd and Fe atoms in Nd_4FeOS_6
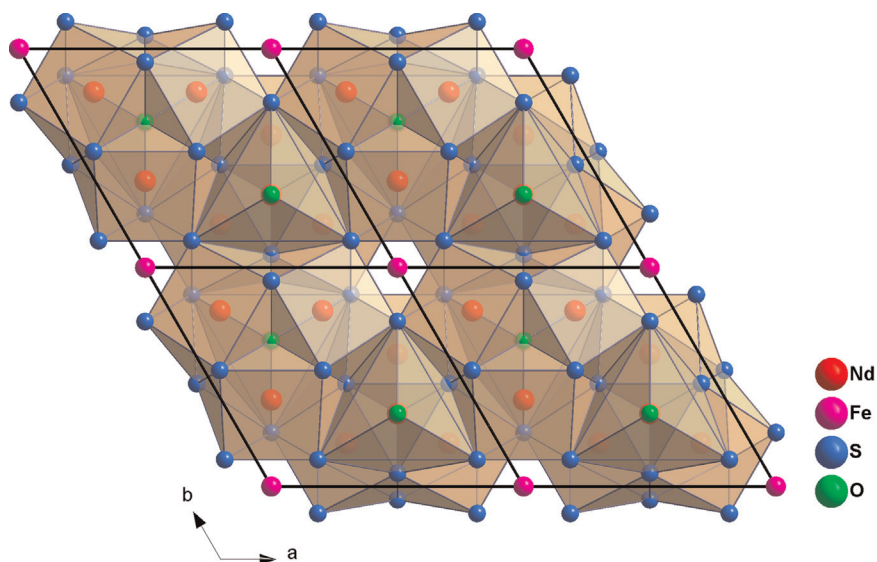
Fig. 2. (001) projection of the structure of Nd_4FeOS_6 represented by a packing of $Nd1S_7O$ and $Nd2S_6O$ polyhedra.

can lead to complex exchange interactions and possible magnetic frustration within the tetrahedra. In particular, although through-space Fe–Fe interactions exist within the $_\propto$ [1] $[FeS_{6 \times 1/2}]^{4-}$ chains, magnetic coupling between Fe atoms could also occur via a through-bond Fe–S1–Fe pathway. Magnetic exchange interactions between neighboring $_\propto$ [1] $[Nd_4OS_3]^{4+}$ chains via Nd1–S2–Nd1 connections ($d_{Nd1-S2}=3.170(2)$ Å) as well as $3d$-$4f$ magnetic exchange interactions could also occur via Nd1–S1–Fe paths ($d_{Nd1-S1}=2.8516(6)$–$2.930(2)$ Å; $d_{Fe-S1}=2.507(2)$–$2.667(3)$ Å) because the Nd1–Fe distance is only 3.3684(8) Å. We will examine possible magnetic structures using electronic structure calculations in a subsequent section.

3.2. Structurally related phases

the La_3CuSiS_7- and the Pr_8CoGa_3-type structures have the same Pearson symbol ($hP24$) and Wyckoff sequence (c^3b^2a) and similar structural motifs as the present Nd_4MnOSe_6-type Nd_4FeOS_6. thus, it is worth comparing these three structural types. to date, the La_3CuSiS_7-type family of structures (space group $P6_3$) consists of more than 250 ternary or quaternary rare earth sulfides and selenides [37]. among these, quaternary phases have a similar formula as the prototype La_3CuSiS_7, in which CU and SI, respectively, occupy the Wyckoff $2a$ (center of the trigonal antiprisms) and one

of the $2b$ sites (center of a tetrahedron). but, the foregoing $2b$ site May also be occupied by a rare earth metal, resulting in the formula R_4TQ_7 (R=rare earth metal, T=transition metal, Q=S or SE). nevertheless, a general principle guiding the formation of this structure type Is that the oxidation states of elements occupying the Wyckoff $2a$ and these $2b$ sites must sum to five, i.e., I–IV and II–III combinations. Sometimes, vacancies can also be introduced if the sum of oxidation states Is more than five, e.g., as seen for $Ce_3Al_{0.67}AlS_7$ [38] and $La_3Mn_{0.5}SiS_7$ [39]. in recent years, discovery of new La_3CuSiS_7-type quaternary phases have aroused considerable interest in the search of multinary 3d/4f chalcogenides [40–45]. considering the vast number of possible combinations for the Wyckoff $2a$ and $2b$ sites and the variety of rare earth metals, a great number of new phases remain, therefore, to be discovered.

The La_3CuSiS_7-type structures differ from the present Nd_4MnOSe_6-type structures mainly by the chains located at (1/3 2/3 z) and equivalent sites. For La_3CuSiS_7-type cases, these chains consist of tetrahedral clusters of chalcogens centered by main group elements (e.g. GaS_4 in Nd_3FeGaS_7) [45] that are bridged by rare earth atoms see Fig. 4(a). For R_4TQ_7 compounds, the chains are built by R-centered tetrahedra (RQ_4) according to databases. However, short R–S distances ($\sim$2.1–2.4 Å) persist for all R_4TQ_7 structures, which were not refined but estimated from isotypic compounds. Since the
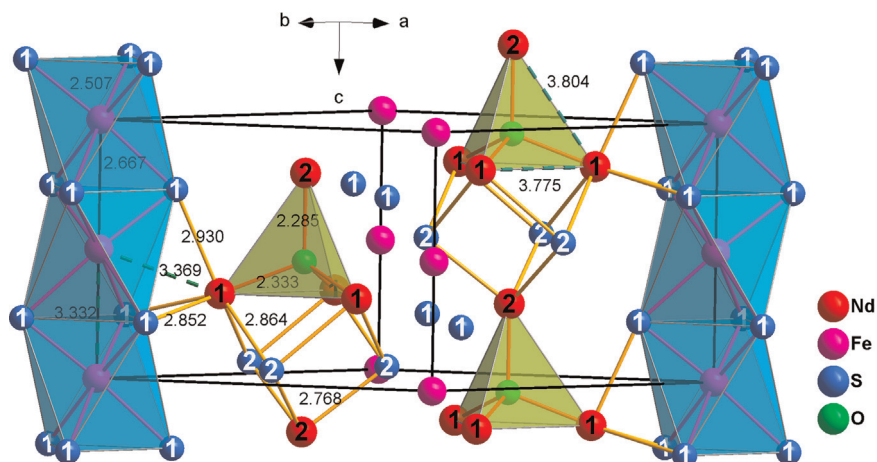

Fig. 3. The structure of Nd_4FeOS_6 represented by a packing of $_\propto^1[FeS_{6x1/2}]^{4-}$ and $_\propto^1[Nd_4OS_3]^{4+}$ chains. The Nd_4O tetrahedra are shaded in lime. For clarity, only two $_\propto^1[FeS_{6x1/2}]^{4-}$ chains are shown with polyhedral clusters (blue). Representative interatomic distances are marked.
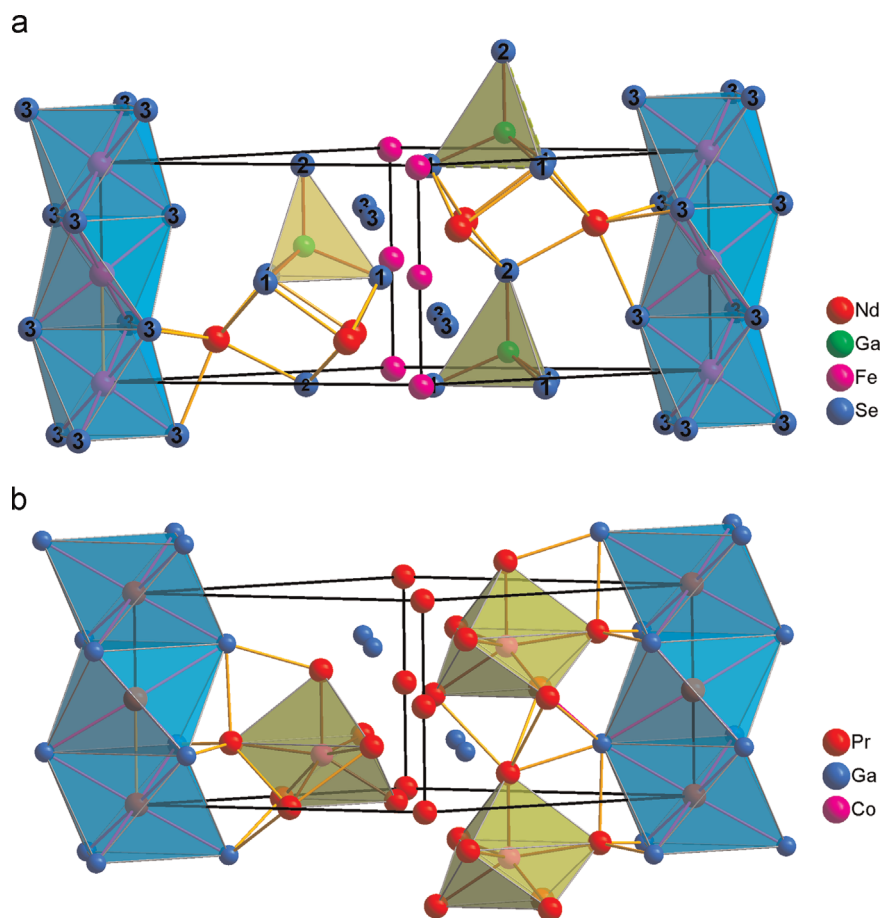
Fig. 4. The structures of (a) La₃CuSiS₇-type Nd₄FeGaSe₆ and (b) Pr₈CoGa₃-type Pr₈CoGa₃.

foregoing distances are typical for R–O rather than R–S bond distances, this outcome questions whether R_4TQ_7 compounds should actually be formally quaternary and contain oxygen; otherwise, proper structural refinements are desired.

On the other hand, reports of Pr₈CoGa₃-type structures include only two series of RE₈CoGa₃ [46] and RE₈CoIn₃, [47] with a total of ~20 members. The Pr₈CoGa₃-type structures exhibit $P6_3mc$ symmetry, the same as Nd₄FeOS₆. Compared to the title compound Nd₄FeOS₆, however, two structural differences are evident for Pr₈CoGa₃-type structures: (1) rare earth metals occupy both the Wyckoff 2*a* and 6*c* sites in Pr₈CoGa₃, whereas Fe and S2 atoms, respectively, occupy these sites in Nd₄FeOS₆ (cf. Fig. 3); and (2) the 2*b* site in the structure of Pr₈CoGa₃, which corresponds to O in Nd₄FeOS₆, is occupied by the transition metal Co and is no longer located at the center of a tetrahedron but, rather, of a mono-capped trigonal prism formed by seven rare earth atoms, Fig. 4(b). The TR₇ clusters (e.g., CoPr₇) could be interesting for their $3d$–$4f$ magnetic interactions. However, to date, no magnetic measurements have been reported for these structures, so, apparently, there is much room for development of new systems with this structure type.

In addition to the above mentioned structural differences, the lattice parameter ratio c/a may be used to differentiate the La₃CuSiS₇-, Pr₈CoGa₃-, and Nd₄MnOSe₆-type structures. As shown in Fig. 5, the c/a ratios for the La₃CuSiS₇-type compounds occur in the range 0.52–0.64; the intermetallic Pr₈CoGa₃-type, 0.66–0.69; and the oxide-containing Nd₄MnOSe₆-type, 0.72–0.73. The c/a value for the title phase is 0.72, falling in the range of the Nd₄MnOSe₆-type structure. This again supports that the
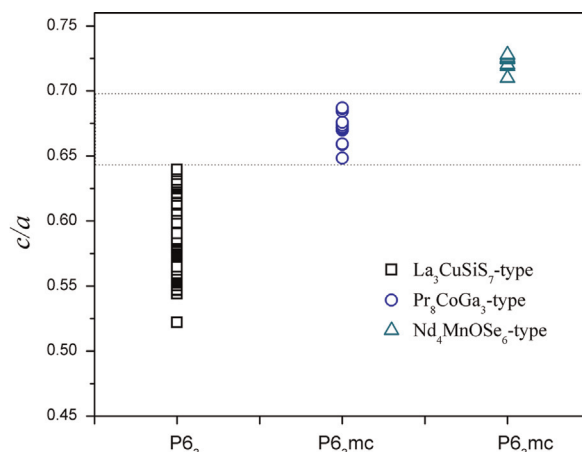

Fig. 5. Distinctive populations of c/a values for the La₃CuSiS₇-, Pr₈CoGa₃-, and Nd₄MnOSe₆-type structures.

assignment of oxygen to the Wyckoff 2*b* site and refined as the Nd₄MnOSe₆-type structure is right.

3.3. Magnetic susceptibility

The temperature dependence of the magnetization was measured on an oriented single crystal with the applied field (H) of 20 Oe, 2 T, and 4 T parallel to the crystal c-axis. No signature of ordering was found down to 2 K, Fig. 6. From the magnetic field
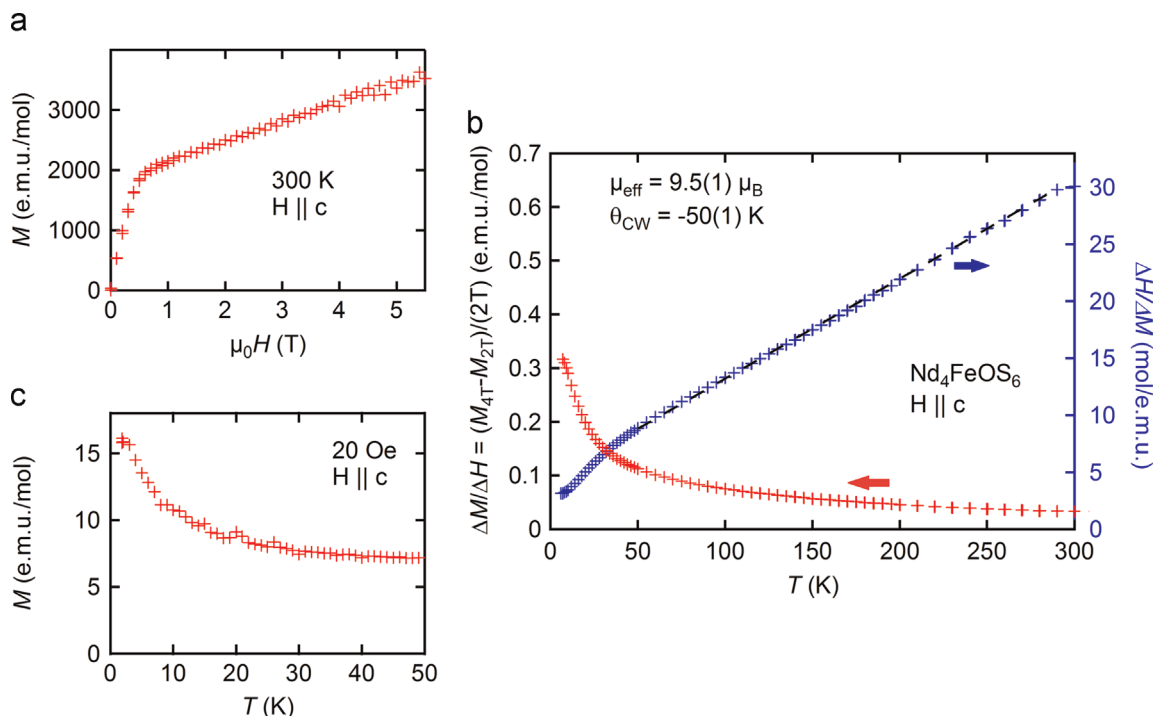
Fig. 6. a) Magnetic field dependence of the magnetization at 300 K for H applied along the c axis. b) temperature dependence of the estimated magnetic susceptibility and its inverse (see text). The dashed line is a Curie–Weiss fit. c) temperature dependence of the magnetization at low temperature for a field of 20 Oe applied along the c axis.

dependence of the magnetization at 300 K (Fig. 6a), we found a significant impurity contribution, which seems to be saturated above 1 T and could originate from residual flux on the surface of the single crystal. Therefore, we used $(\Delta M/\Delta H)=(M_{4T}-M_{2T})/(2\,T)$ to estimate the susceptibility. After this treatment, the inverse susceptibility shows a linear temperature dependence above 40 K (see Fig. 6b). A fit of the data yields a Curie–Weiss temperature of $\theta_{CW} \approx -50$ K and an effective moment of 9.5(1) μ_B/f.u. If both Nd^{3+} and Fe^{2+} ions contribute a moment of 3.62 μ_B and 4.90 μ_B, respectively, the expected effective moment would be 8.74 μ_B/f.u. according to the equation $\mu_{eff} = \sqrt{4(3.62^2) + 1(4.90^2)}\,\mu_B$. This value is marginally close to the experimental value from our data considering the fact that we can only estimate the susceptibility due to the contribution of impurities. Crystal electric field effects can also affect the measured value on single crystals. The negative Curie–Weiss temperature $(\theta_{CW} \approx -50$ K) indicates antiferromagnetic interactions within Nd_4FeOS_6, a result that is consistent with theoretical calculations (below). In fact, several La_3CuSiS_7-type and related phases without oxygen also show either very low or no magnetic ordering temperature [42–45]. Interestingly, all Nd-containing Nd_3TGaQ_7 (T=Fe, Co; Q=S, Se) compounds have large negative Curie–Weiss temperatures, but they remain paramagnetic down to low temperatures [43]. We note, though, that the crystal electric field can modify the value of the Curie–Weiss temperature on single crystals.

3.4. Electronic structure

As mentioned above, Nd_4FeOS_6 exhibited antiferromagnetic (AFM) interactions from the Curie–Weiss temperature of –50 K, but no ordering phenomena were observed down to 2 K. These suggest that dominant exchange interactions are of antiferromagnetic (AFM) character. To obtain insights about possible magnetic exchange interactions in Nd_4FeOS_6, a total of six magnetically ordered models (see Fig. 7) were examined, including one ferromagnetic (FM) model, one ferrimagnetic (Fi) model with opposite spins between Nd and Fe atoms, and four

antiferromagnetic (AFM1-AFM4) models. Due to the overall structural complexity, the repeat unit of each model was limited to one crystallographic unit cell, that is, a focus on 8 Nd^{3+} and 2 Fe^{2+} sites, although other AFM models could also occur as superstructures. The results of this analysis are summarized in Table 4.

Among these six models, one of the antiferromagnetic models, AFM4, has the lowest total energy, in agreement with the assessment from the Curie–Weiss temperature. Fig. 8 shows the spin-polarized DOS curve for model AFM4. The Nd 4f majority spin states are partially occupied between –4.5 eV and –3.0 eV, whereas the remaining majority and minority spin 4f states are located between +2.0 and +3.0 eV. The integrated areas for the occupied and unoccupied majority spin states have a ratio of 3:4, indicating a high spin f^3 configuration. As for the Fe 3d states, the majority spin orbitals are located between –5.3 eV and –3.0 eV, while its minority spin orbitals occur between +1.5 eV and +3.0 eV, with some being in the occupied energy range of –0.7 eV relative to E_F, indicating a high spin d^6 configuration for each Fe atom, i.e., Fe^{2+}.

Five spin exchange parameters within Nd_4FeOS_6 were evaluated by performing a mapping analysis [48–50] on the basis of the six ordered models shown in Fig. 7. As indicated also in Fig. 7, the five spin exchange paths of Nd_4FeOS_6 include the intra-cluster Nd–Nd interactions within a [Nd_4O] tetrahedron (J_1), inter-cluster Nd–Nd interactions within the chains (J_2), inter-chain Nd–Nd (J_3) and Nd–Fe (J_4) interactions, and inter-cluster Fe–Fe (J_5) interactions. The relative energies, per formula units (f.u.), of the six models were determined from our VASP (GGA+U) calculations as summarized in Fig. 7. The energies of these models can also be approximated in terms of the spin Hamiltonian,

$$\hat{H} = -\sum_{i<j} J_{ij}\,\hat{S_i}\,\hat{S_j},$$

in which J_{ij} is the spin exchange parameter for the interaction between the spin sites i and j. By applying this energy expression for spin dimers with N unpaired spins per spin site ($N_{Nd}=3$ for high-spin Nd^{3+} and $N_{Fe}=4$ for high-spin Fe^{2+}), [48–50] the total
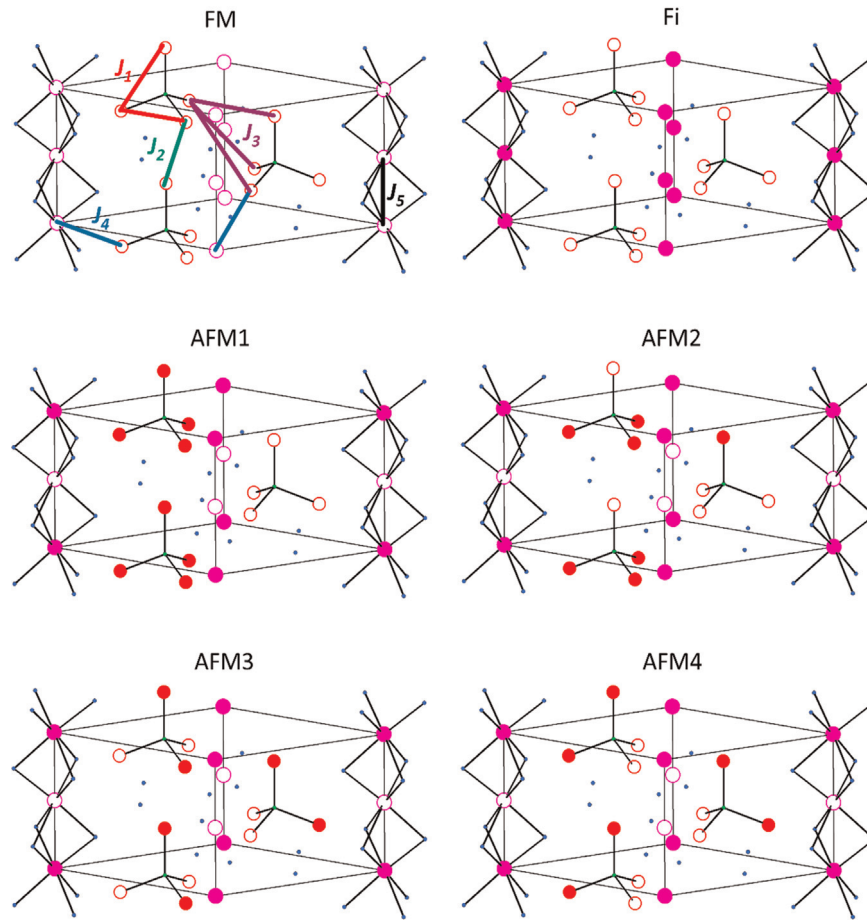
Fig. 7. Six magnetic structural models of Nd_4FeOS_6 used for calculations in this work. Red, purple, blue and green circles represent Nd, Fe, S and O atoms, respectively. Solid and empty spheres denote oppositely oriented magnetic spins of Nd and Fe. The size of nonmagnetic S and O atoms are intentionally scaled to be small. The five spin exchange paths of Nd_4FeOS_6 (J_1–J_5) are showed in the FM model. J_1 is an average of two intra-cluster Nd–Nd spin exchange parameters. J_3 is an average of three inter-chain Nd–Nd spin exchange parameters. J_4 is an average of two inter-chain Nd–Fe spin exchange parameters.

Table 4
Magnetic moments on Nd and Fe, total energies and spin exchange energy expressions for the six magnetic structures models of Nd_4FeOS_6.

| Magnetic moments			Energy[*]	Spin exchange energy expression
	μ_{Nd} (μ_B)	μ_{Fe} (μ_B)	(meV/f.u.)	(meV)
FM	3.01	3.51	127.6	$\frac{N_{Nd}^2}{4}\left(-6J_1 - 3J_2 - 18J_3\right) - \frac{N_{Nd}\,N_{Fe}}{4}\left(6J_4\right) - \frac{N_{Fe}^2}{4}\left(J_5\right)$
Fi	2.99	−3.54	563.1	$\frac{N_{Nd}^2}{4}\left(-6J_1 - 3J_2 - 18J_3\right) + \frac{N_{Nd}\,N_{Fe}}{4}\left(6J_4\right) - \frac{N_{Fe}^2}{4}\left(J_5\right)$
AFM1	± 3.00	± 3.49	504.1	$\frac{N_{Nd}^2}{4}\left(-6J_1 - 3J_2 - 18J_3\right) + \frac{N_{Fe}^2}{4}\left(J_5\right)$
AFM2	± 2.99	± 3.52	120.6	$\frac{N_{Nd}^2}{4}\left(3J_2 + 6J_3\right) + \frac{N_{Fe}^2}{4}\left(J_5\right)$
AFM3	± 3.00	± 3.53	31.9	$\frac{N_{Nd}^2}{4}\left(2J_1 + J_2 + 2J_3\right) + \frac{N_{Fe}^2}{4}\left(J_5\right)$
AFM4	± 3.00	± 3.53	0.0	$\frac{N_{Nd}^2}{4}\left(2J_1 + J_2 - 2J_3\right) + \frac{N_{Fe}^2}{4}\left(J_5\right)$
J (meV)	$J_1 = -27.6, J_2 = -15.0, J_3 = +3.6, J_4 = +12.1, J_5 = +20.0$			

[*] Total energy relative to model AFM4 from VASP calculation

spin exchange energies of the six models are summarized in Table 4. Thus, by mapping the relative energies of the six models determined by the VASP (GGA+U) calculations onto the corresponding relative energies determined from the above spin exchange energies,[48–50] we obtained the values of J_{ij} listed in the

last line of Table 4. These parameters indicate that the intra-chain Nd–Nd interactions, J_1 (−27.6 meV) and J_2, (−15.0 meV) are substantially antiferromagnetic. Considering the tetrahedral geometry for Nd_4O, intra-chain AFM Nd–Nd couplings must lead to magnetic frustration among Nd atoms. Moreover, the frustration could affect
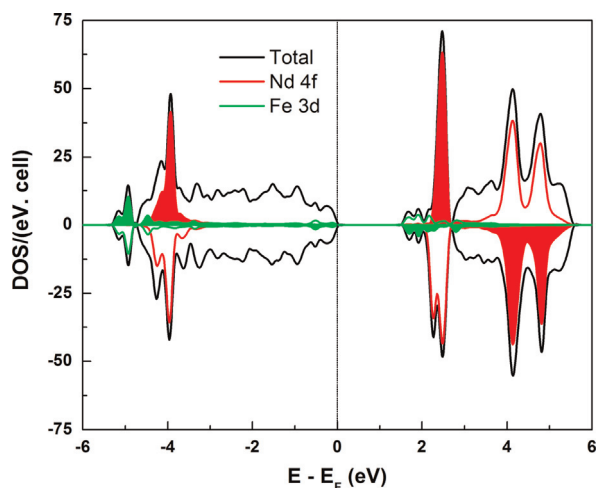
Fig. 8. Total and partial density-of-states (DOS) of an antiferromagnetic model of Nd$_4$FeOS$_6$. Contributions from Nd and Fe atoms with positive moments are shaded. The white areas within –4.0 to 0 eV are dominated by the p states of O and S.

the magnetic ordering associated with Fe sites because Nd–Fe coupling is also strong FM ($J_4 = +12.1$ meV). Therefore, Nd$_4$FeOS$_6$ can be considered to be a complex, magnetically frustrated system, which, in turn, leads to the absence of magnetic ordering down to 2 K.

4. Conclusions

In this work, single crystals of Nd$_4$FeOS$_6$ ($P6_3mc$, $a = 9.2693(1)$ Å, $c = 6.6650(1)$ Å, $V = 495.94(1)$ Å^3, $Z = 2$) have been unexpectedly grown in an attempt to get ternary Nd–Fe–S phases using the eutectic Fe–S solution as a self-flux. The presence of a low percentage of oxygen atoms being trapped by rare earth [Nd$_4$] tetrahedra reinforces the notion that contamination by oxygen for the preparation of many rare earth materials should always be considered. Nevertheless, the title phase exhibits a stunning structural motif of parallel chains of face-sharing trigonal antiprisms of [FeS$_{6/3}$]$^{4-}$ and interlinked cubane-like clusters of [Nd$_4$OS$_3$]$^{4+}$. Although oxygen, sulfur, and selenium are in the same group, the trapping of oxygen by rare earth tetrahedra distinguishes the structure of Nd$_4$MnOSe$_6$-type Nd$_4$FeOS$_6$ from related La$_3$CuSiS$_7$- and Pr$_8$CoGa$_3$-type structures containing only sulfur or selenium. According to magnetic susceptibility measurements, Nd$_4$FeOS$_6$ exhibits net antiferromagnetic interactions, but no antiferromagnetic ordering temperature down to 2 K, a result that is likely due to complex magnetic frustration as suggested by theory. Spin-polarized electronic structure calculations also confirm that antiferromagnetic interactions are more energetically favorable than ferromagnetic ones. In addition, high spin states for Nd^{3+} (4f^3) and Fe^{2+} (3d^6) ions are suggested.

Acknowledgements

Appendix A. Supplementary material

Supplementary data associated with this article can be found in the online version at 10.1016/j.jssc.2015.05.020.

References

[1] M.D. Kuz'min, A.M. Tishin, Handb. Magn. Mater. 17 (2007) 149–233.
[2] F. Canepa, Recent Res. Dev. Magn. Magn. Mater. 1 (2003) 67–99.
[3] B.R. Coles, Physica B (Amsterdam) 163 (1990) 741–743.
[4] F.R. De Boer, K.H.J. Buschow, Physica B (Amsterdam) 177 (1992) 199–206.
[5] M. Richter, J. Phys. D: Appl. Phys. 31 (1998) 1017–1048.
[6] O. Costisor, W. Linert, Trends Inorg. Chem. 8 (2005) 89–106.
[7] J.J.M. Franse, F.E. Kayzel, N.P. Thuy, J. Magn. Magn. Mater. 129 (1994) 26–38.
[8] C. Mathoniere, J.-P. Sutter, J.V. Yakhmi, Bimetallic Magnets Present and Perspectives, Wiley-VCH Verlag GmbH & Co. KGaA (2003), p. 1–40.
[9] A. Szytula, J. Leciejewicz, Handbook of Crystal Structures and Magnetic Properties of Rare Earth Intermetallics, CRC Press, Boca Raton, Fl, 1994.
[10] P.C. Dent, J. Appl. Phys. 111 (2012) 07A721/1-07A721/6.
[11] X. Lin, V. Taufour, S.L. Bud'ko, P.C. Canfield, Philos. Mag. 94 (12) (2014) 1277–1300.
[12] P.C. Canfield, Book Series Complex Metellaic Alloys, World Scientific Publishing Co. Pte. Ltd. (2010), p. 93–111.
[13] P.C. Canfield, Z. Fisk, Philos. Mag. Part B 65 (6) (1992) 1117–1123.
[14] J.P.A. Westerveld, D.M.R. Lo Cascio, M.O. Doornik, P.I. Loeff, H. Bakker, H.J. M. Heijligers, G.F. Bastin, J. Less-Common Met. 146 (189-95) (1989).
[15] G. Collin, F. Rouyer, J. Loriers, C. R. Acad. Sci. Paris, Chimie 266 (1968) 689–691.
[16] T. Schleid, F. Lissner, J. Less Common Metals 175 (2) (1991) 309–319.
[17] I. Ijjaali, B. Deng, J.A. Ibers, J. Solid State Chem. 178 (5) (2005) 1503–1507.
[18] Bruker, SAINT plus. Version 8.30, Bruker AXS Inc., Madison, Wisconsin, USA, 2013.
[19] G.M. Sheldrick, SADABS, University of Grottingen, Germany, 1996.
[20] SHELXTL, 6.10 ed., Bruker Analytical X-ray Systems, Inc., Madison, WI. 2000.
[21] A.L. Spek, J. Appl. Cryst. 36 (2003) 7–13.
[22] L.M. Gelato, E. Parthé, J. Appl. Crystallogr. 20 (1987) 139–143.
[23] P.E. Blöchl, Phys. Rev. B 50 (24) (1994) 17953–17979.
[24] G. Kresse, D. Joubert, Phys. Rev. B 59 (3) (1999) 1758–1775.
[25] G. Kresse, J. Furthmüller, Comput. Mater. Sci. 6 (1) (1996) 15–50.
[26] G. Kresse, J. Furthmüller, Phys. Rev. B 54 (16) (1996) 11169–11186.
[27] J.P. Perdew, K. Burke, M. Ernzerhof, Phys. Rev. Lett. 77 (18) (1996) 3865–3868.
[28] S.L. Dudarev, G.A. Botton, S.Y. Savrasov, C.J. Humphreys, A.P. Sutton, Phys. Rev. B 57 (1998) 1505–1509.
[29] B.N. Harmon, V.P. Antropov, A.I. Liechtenstein, I.V. Solovyev, V.I. Anisimov, J. Phys. Chem. Solids 56 (1995) 1521–1524.
[30] D. Paudyal, V.K. Pecharsky, K.A. Gschneidner, J. Appl. Phys. (Melville, NY, U. S.) 115 (2014) 17E127/1-17E127/3.
[31] S. Sportouch, C. Belin, M. Tillard-Charbonnel, Acta Crystallogr., Sect. C: Cryst. Struct. Commun. C50 (1994) 1861–1862.
[32] Y. Ohki, K. Tanifuji, N. Yamada, R.E. Cramer, K. Tatsumi, Chem. -Asian J. 7 (2012) 2222-2224, S2222/1-S2222/9.
[33] M. Kodaka, T. Tomohiro, K. Uoto, H. Okuno, Trends Org. Chem. 1 (1990) 127–139.
[34] J.X. Boucherle, J. Schweizer, Acta Crystallogr. B 31 (11) (1975) 2745–2746.
[35] M.G. Kanatzidis, R. Pottgen, W. Jeitschko, Angew. Chem., Int. Ed. 44 (2005) 6996–7023.
[36] I.D. Brown, D. Altermatt, Acta Crystallogr. Section B 41 (4) (1985) 244–247.
[37] P. Villars, L.D. Calvert, Pearson's Handbook of Crystallographic Data for Intermetallic Phases Vol. 1, 2nd ed., American Society of Metals, Metals Materials Park, OH, 1991.
[38] M. Patrie, M. Guittard, C. R. Acad. Sci., Ser. IIC: C 268 (1969) 1136–1138.
[39] G. Collin, P. Laruelle, C. R. Acad. Sci., Ser. IIC: C 270 (1970) 410–412.
[40] M. Daszkiewicz, L.D. Gulay, O.S. Lychmanyuk, A. Pietraszko, J. Alloy. Compd. 467 (1–2) (2009) 168–172.
[41] M. Daszkiewicz, L.D. Gulay, A. Pietraszko, V.Y. Shemet, J. Solid State Chem. 180 (7) (2007) 2053–2060.
[42] B.W. Rudyk, S.S. Stoyko, A. Mar, J. Solid State Chem. 208 (0) (2013) 78–85.
[43] B.W. Rudyk, S.S. Stoyko, A.O. Oliynyk, A. Mar, J. Solid State Chem. 210 (1) (2014) 79–88.
[44] W. Yin, Y. Shi, B. Kang, J. Deng, J. Yao, Y. Wu, J. Solid State Chem. 213 (2014) 87–92.
[45] W. Yin, W. Wang, L. Kang, Z. Lin, K. Feng, Y. Shi, W. Hao, J. Yao, Y. Wu, J. Solid State Chem. 202 (0) (2013) 269–275.
[46] Y.N. Grin, O.M. Sichevich, R.E. Gladyshevskii, Y.P. Yarmolyuk, Kristallografiya 29 (1984) 708–711.
[47] M. Dzevenko, I. Bigun, M. Pustovoychenko, L. Havela, Y. Kalychak, Intermetallics 38 (2013) 14–18.
[48] D. Dai, M.-H. Whangbo, J. Chem. Phys. 114 (7) (2001) 2887–2893.
[49] D. Dai, M.-H. Whangbo, J. Chem. Phys. 118 (1) (2003) 29–39.
[50] M.-H. Whangbo, H.-J. Koo, D. Dai, J. Solid State Chem. 176 (2) (2003) 417–481.